quantum dot is also a powerful tool to investigate quasi-particle–related limitations on the performance of superconducting qubits (*28*, *31*, *32*) and detectors (*33*). Furthermore, our experimental strategy could be used to explore hybrid superconducting devices in the regime where Andreev states evolve into Majorana states (*34*–*36*).

REFERENCES AND NOTES

1. K. J. Franke, G. Schulze, J. I. Pascual, *Science* **332**, 940–944 (2011).
2. C. Caroli, P. G. de Gennes, J. Matricon, *Phys. Lett.* **9**, 307–309 (1964).
3. C. W. J. Beenakker, H. van Houten, *Phys. Rev. Lett.* **66**, 3056–3059 (1991).
4. M. A. Despósito, A. Levy Yeyati, *Phys. Rev. B* **64**, 140511(R) (2001).
5. A. Zazunov, V. S. Shumeiko, E. N. Bratus', J. Lantz, G. Wendin, *Phys. Rev. Lett.* **90**, 087003 (2003).
6. N. M. Chtchelkatchev, Yu. V. Nazarov, *Phys. Rev. Lett.* **90**, 226806 (2003).
7. A. Zazunov, V. S. Shumeiko, G. Wendin, E. N. Bratus', *Phys. Rev. B* **71**, 214505 (2005).
8. C. Padurariu, Yu. V. Nazarov, *Europhys. Lett.* **100**, 57006 (2012).
9. J.-D. Pillet *et al.*, *Nat. Phys.* **6**, 965–969 (2010).
10. M. Zgirski *et al.*, *Phys. Rev. Lett.* **106**, 257003 (2011).
11. E. M. Levenson-Falk, F. Kos, R. Vijay, L. Glazman, I. Siddiqi, *Phys. Rev. Lett.* **112**, 047002 (2014).
12. A. Zazunov, A. Brunetti, A. Levy Yeyati, R. Egger, *Phys. Rev. B* **90**, 104508 (2014).
13. L. Bretheau, Ç. Ö. Girit, H. Pothier, D. Esteve, C. Urbina, *Nature* **499**, 312–315 (2013).
14. L. Bretheau, Ç. Ö. Girit, C. Urbina, D. Esteve, H. Pothier, *Phys. Rev. X* **3**, 041034 (2013).
15. E. Scheer, P. Joyez, D. Esteve, C. Urbina, M. H. Devoret, *Phys. Rev. Lett.* **78**, 3535–3538 (1997).
16. J. M. van Ruitenbeek *et al.*, *Rev. Sci. Instrum.* **67**, 108 (1996).
17. C. Janvier *et al.*, *J. Phys. Condens. Matter* **26**, 474208 (2014).
18. A. Wallraff *et al.*, *Nature* **431**, 162–167 (2004).
19. G. Romero, I. Lizuain, V. S. Shumeiko, E. Solano, F. S. Bergeret, *Phys. Rev. B* **85**, 180506 (2012).
20. Materials and methods are available as supplementary materials on *Science* Online.
21. D. G. Olivares *et al.*, *Phys. Rev. B* **89**, 104504 (2014).
22. R. Vijay, D. H. Slichter, I. Siddiqi, *Phys. Rev. Lett.* **106**, 110502 (2011).
23. M. Greenfeld, D. S. Pavlichin, H. Mabuchi, D. Herschlag, *PLOS ONE* **7**, e30024 (2012).
24. J. M. Martinis, M. Ansmann, J. Aumentado, *Phys. Rev. Lett.* **103**, 097002 (2009).
25. G. Catelani, R. J. Schoelkopf, M. H. Devoret, L. I. Glazman, *Phys. Rev. B* **84**, 064517 (2011).
26. F. Kos, S. E. Nigg, L. I. Glazman, *Phys. Rev. B* **87**, 174521 (2013).
27. I. M. Pop *et al.*, *Nature* **508**, 369–372 (2014).
28. C. Wang *et al.*, *Nat. Commun.* **5**, 5836 (2014).
29. Y. Makhlin, A. Shnirman, *Phys. Rev. Lett.* **92**, 178301 (2004).
30. J. Clarke, F. K. Wilhelm, *Nature* **453**, 1031–1042 (2008).
31. U. Vool *et al.*, *Phys. Rev. Lett.* **113**, 247001 (2014).
32. D. Ristè *et al.*, *Nat. Commun.* **4**, 1913 (2013).
33. P. J. de Visser *et al.*, *Phys. Rev. Lett.* **106**, 167004 (2011).
34. W. Chang, V. E. Manucharyan, T. S. Jespersen, J. Nygård, C. M. Marcus, *Phys. Rev. Lett.* **110**, 217005 (2013).
35. V. Mourik *et al.*, *Science* **336**, 1003–1007 (2012).
36. D. Chevallier, P. Simon, C. Bena, *Phys. Rev. B* **88**, 165401 (2013).

ACKNOWLEDGMENTS

We thank P. Sénat and P.-F. Orfila for technical assistance and G. Catelani, V. Shumeiko, and A. Levy Yeyati for discussions. We acknowledge financial support by contract ANR-12-BS04-0016-MASH. Ç.Ö.G. was supported by the People Programme (Marie Curie Actions) of the European Union's Seventh Framework Programme (FP7/2007-2013) under Research Executive Agency grant agreement PIIF-GA-2011-298415. L.T. was supported by ECOS-SUD (France-Argentina) grant A11E04 and a scholarship from CONICET (Argentina). C.J., M.F.G., H.P., and C.U. took part in all aspects of this work. L.T., L.B., Ç.Ö.G., and D.E. participated in the design of the experiment. M.S. and D.V. helped with microwave setup. L.T. and D.V. participated in running the experiment. All authors participated in interpreting the data and writing the manuscript.

SUPPLEMENTARY MATERIALS

www.sciencemag.org/content/349/6253/1199/suppl/DC1
Materials and Methods
Figs. S1 to S9
Movie S1

27 March 2015; accepted 30 July 2015
10.1126/science.aab2179

CRITICAL PHENOMENA

Critical behavior at a dynamic vortex insulator-to-metal transition

Nicola Poccia,[1,2] Tatyana I. Baturina,[3,4,5] Francesco Coneri,[1] Cor G. Molenaar,[1] X. Renshaw Wang,[1] Ginestra Bianconi,[6] Alexander Brinkman,[1] Hans Hilgenkamp,[1] Alexander A. Golubov,[1,7] Valerii M. Vinokur[5]*

An array of superconducting islands placed on a normal metal film offers a tunable realization of nanopatterned superconductivity. This system enables investigation of the nature of competing vortex states and phase transitions between them. A square array creates the eggcrate potential in which magnetic field–induced vortices are frozen into a vortex insulator. We observed a vortex insulator–vortex metal transition driven by the applied electric current and determined critical exponents that coincided with those for thermodynamic liquid-gas transition. Our findings offer a comprehensive description of dynamic critical behavior and establish a deep connection between equilibrium and nonequilibrium phase transitions.

Critical behaviors near phase transitions can be classified into universality classes determined only by a few properties characterizing the system, such as space dimensionality, range of interaction, and symmetry (*1*, *2*). A paradigmatic concept of universality brought deep understanding of equilibrium critical phenomena [see, e.g., (*3*) and references therein]. Phase transitions and criticality far from equilibrium are less well understood. The experimental evidence for universality of nonequilibrium phase transitions is still scarce, calling for intensified experimental efforts.

Superconducting vortices offer a unique tunable laboratory for studying classical critical dynamics. To that end, we prepared an array of superconducting islands where vortices are pinned between the islands in the areas of weaker proximity-induced superconductivity—that is, at the energy dimples of an eggcrate potential (*4*). If thermal fluctuations are not strong enough to overcome the combined localizing action of mutual repulsion and pinning, vortices form the so-called vortex Mott insulating state at commensurate fields corresponding to an integer number of vortices per pinning site (*5*). The predicted vortex Mott state seen in experiments on antidot arrays in superconducting films (*6*, *7*) was conclusively confirmed in (*8*). In our experiment, performed in a classical regime, varying the magnetic field provides precise control over the vortex density and tunes the ratio of the vortex repulsion to the mobility, enabling the observation of a vortex insulator-to-metal transition.

Each of our samples consists of a 40-nm Au layer, patterned as a four-point setup in a van der Pauw configuration for transport measurements, on a Si/SiO_2 substrate (*9*). The Au pattern is overlaid with a square array of superconducting niobium (Nb) islands 45 nm thick. An array contains 90,000 Nb islands placed with a period $a = 267$ nm. The diameter of an island is 220 ± 3 nm and the island separation is 47 ± 3 nm. Shown in Fig. 1, A to D, are scanning electron microscopy (SEM), atomic force microscopy (AFM), and optical images of a sample and the height profile along one of the principal axes of the array. The superconducting transition temperature of the array, determined as the midpoint of the temperature resistance curve in the upper inset in Fig. 1A, is $T_c = 7.3$ K, which is 2 K lower than that of bulk Nb ($T_{c0} = 9.3$ K). This implies that the array is a strongly coupled network of superconducting islands (*10*–*12*). The parameters of our array ensure that the intersite barriers are high enough to provide pinning sufficient for formation of the vortex Mott insulator state and that vortex motion is thermally activated.

The measurements are carried out in a shielded cryostat at temperature $T = 1.4$ K. Figure 2A shows

[1]MESA+ Institute for Nanotechnology, University of Twente, 7500 AE Enschede, Netherlands. [2]Rome International Center for Materials Science Superstripes (RICMASS), Via dei Sabelli 119A, 00185 Roma, Italy. [3]A. V. Rzhanov Institute of Semiconductor Physics, Siberian Branch of the Russian Academy of Sciences, Novosibirsk 630090, Russia. [4]Novosibirsk State University, Novosibirsk 630090, Russia. [5]Materials Science Division, Argonne National Laboratory, Argonne, IL 60637, USA. [6]School of Mathematical Sciences, Queen Mary University of London, London E1 4NS, UK. [7]Moscow Institute of Physics and Technology, Dolgoprudnyi, Moscow District, Russia.
***Corresponding author. E-mail: vinokour@anl.gov**

color plots of the differential resistance, dV/dI, as a function of the applied current and the magnetic field in units of frustration parameter $f = B/B_0$, where $B_0 = \Phi_0/a^2 = 28.6$ mT, and $\Phi_0 = \pi\hbar/e$ is the magnetic flux quantum. Figure 2B displays representative isocurrent cuts as dV/dI versus B.

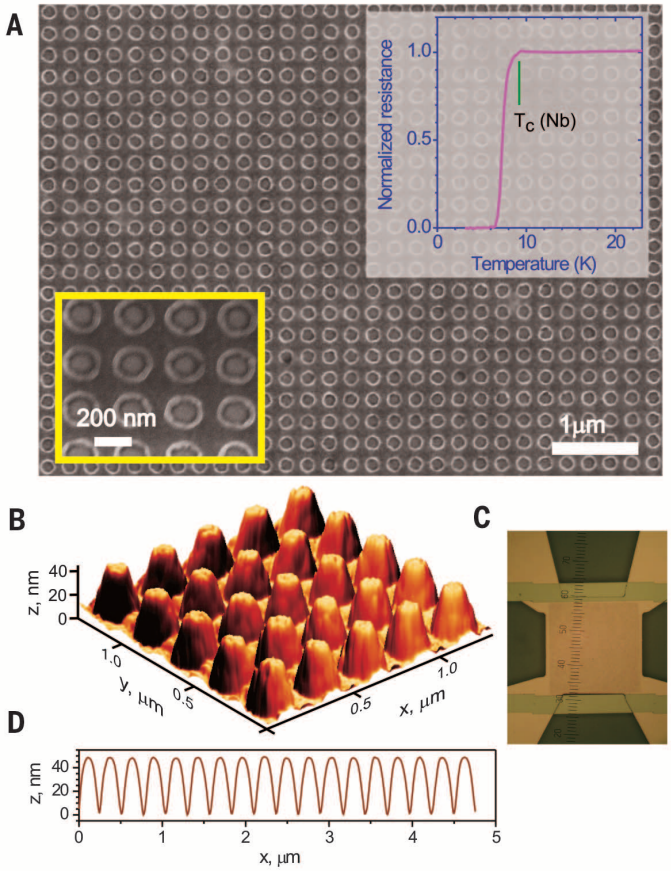

Fig. 1. Experimental setup. (**A**) SEM image of the square array of Nb islands on Au. The inset at lower left is a magnified image of the array. The inset at upper right shows the temperature dependence of the resistance near the superconducting transition T_c of bulk Nb (marked by the vertical bar). (**B**) 1.4 μm × 1.4 μm AFM topography of the superconductor islands on the metallic template of the same sample. (**C**) Optical image of the Au template with four contacts (yellow), Nb bus bars (light green), and the array of 300 × 300 Nb islands barely visible as a red square shadow on a Si/SiO_2 substrate (dark green). (**D**) Height profile along the principal axis of the array.

At modest currents, the data reveal a wealth of dips in dV/dI at integer frustrations, namely at $f = 1$, 2, and 3 (corresponding to integer numbers of flux quanta per elemental square of an array), as well as a fine structure of fractional dips at $f = {}^1/_3, {}^1/_2, {}^2/_3, {}^4/_3, {}^3/_2, \ldots$. These minima reflect the modulation of the ground-state energy E_g due to formation of periodic vortex patterns in a magnetic field (Fig. 2, C and D). The energy spectrum of the fractional vortex Mott insulator shown in Fig. 2C is the Hofstadter butterfly spectrum of the Harper equation (*13*). The dips in the resistance and singularities in magnetization at commensurate frustrations were observed in numerous experiments [see (*14*) and references therein].

Our key observation is a reversal of the minima in dV/dI into maxima at rational f upon increasing the current bias. Scaling analysis (see below) shows that this is a direct manifestation of the existence of the vortex Mott insulator and its transition into a metallic state. Reversals at commensurate fields $f_c = {}^1/_3, {}^1/_2, {}^2/_3, 1, \ldots$ are most pronounced at integer and half-integer frustration factors (Fig. 2B). The insulating behavior appears as a tendency to downward divergence of the dV/dI traces on approach to f_c. Upon the vortex Mott insulator-to-metal transition with the increasing current, an upward divergence of dV/dI traces marks the metallic-like dV/dI behavior near f_c. Figure 3 shows the plots of dV/dI versus B in the vicinity of $f_c = {}^1/_2$, 1, 2. Similar minima-to-maxima flips were observed in regular superconducting systems of different geometries (*15*, *16*). However, the mechanism of current-stimulated depinning proposed in (*15*, *16*) would lead to disappearance of the dips in the resistance $R = V/I$ responsible for the dissipation, and not only in dV/dI. This is not the case in our

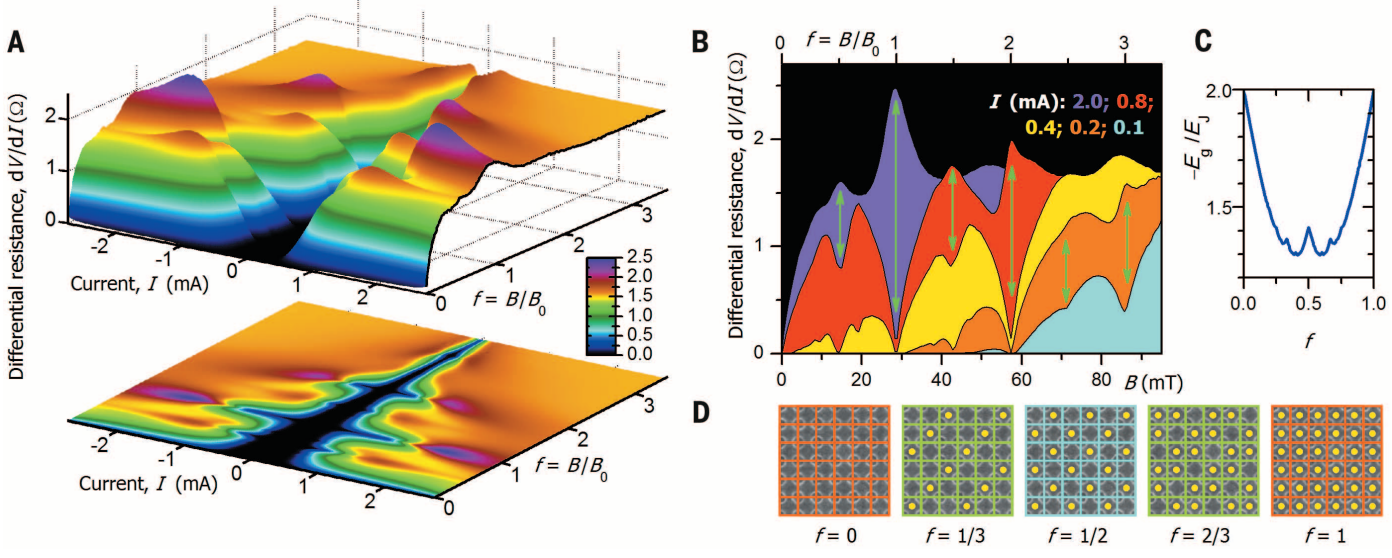

Fig. 2. Vortex Mott insulator-to-metal transition. (**A**) Color plots of dV/dI versus current and magnetic field. The color scale indicates dV/dI values in ohms. (**B**) Representative dV/dI versus $f = B/B_0$ curves at different bias currents. At low current bias (blue, orange, and yellow), dV/dI minima at $f = {}^1/_3, {}^1/_2, {}^2/_3, 1, {}^4/_3, {}^3/_2, {}^5/_3, 2, {}^7/_3, {}^5/_2, {}^8/_3$, and 3 indicate formation of a vortex Mott insulator. Increasing current reverses minima into maxima (red and violet). Reversals manifesting the insulator-to-metal transition are highlighted by vertical arrows. (**C**) Ground-state energy E_g versus f obtained from the Harper equation (*14*, *23*). (**D**) Vortex configurations at rational frustrations $f = 0$, ${}^1/_3$, ${}^1/_2$, ${}^2/_3$, and 1. Periodic arrays of vortices (yellow circles) are superimposed on the SEM subimages of the square array of Nb islands.

experiment (see fig. S1). The resistance exhibits pronounced dips indicating strong pinning at rational f even at the currents where dV/dI shows profound maxima. Hence, the dip-to-maxima flips cannot be explained as vortex depinning.

Shown in the upper row of Fig. 3 are detailed plots of dV/dI versus B in the vicinity of $f_c = {}^1/_2$, 1, 2. There are separatrices, $I_0^{\pm}$, highlighted by dots in Fig. 3, A to C, dividing insulating-like and metallic-like curves. We identify $I_0^{\pm}$ as critical currents at which the dynamic vortex Mott transition occurs, and find them from the condition $d(dV/dI)/df|_{f=f_c^{\pm}} = 0$. For $I > I_0^{\pm}$ the dV/dI traces display minima, marked by strokes in Fig. 3, A to C. That I_0^- and I_0^+ are different implies that in the current intervals $I \in (\min\{I_0^-, I_0^+\}, \max\{I_0^-, I_0^+\})$ at commensurate values f, vortex Mott insulating and metallic phases coexist (*17*).

Now we turn to the proximity of the vortex insulator-to-metal transition critical point, (I_0, f_c). We conjecture mapping of the variables describing the critical behavior of the static electronic Mott transition to those of the dynamic vortex Mott transition (*9*): $|U - U_c| \to b = |f_c - f|$, $|T - T_c| \to |I - I_0|$, and the critical point $(T_c, U_c) \to (I_0, f_c)$, yielding critical scaling $|I - I_0| \propto |b|^{\varepsilon}$. To demonstrate the critical behavior, we scale dV/dI data into the universal form

$$\frac{dV(f,I)}{dI} - \left[\frac{dV(f,I)}{dI}\right]_{I=I_0} = F_{\pm}\left(\frac{|I - I_0^{\pm}|}{|b|^{\varepsilon}}\right) \quad (1)$$

where ε is an adjustable parameter. The best fit of the data near $f_c = {}^1/_2$ is achieved at $\varepsilon = {}^1/_2$ (Fig. 3D). The same procedure for the left and right sides of $f_c = 1$ and 2 gives rise to $\varepsilon = {}^2/_3$ (Fig. 3, E and F). Double-logarithmic plots in the vicinity of the above values of f_c display a power-law functional form of $F_{\pm}(x) \propto x^{\mu}$, as shown in the lower panels of Fig. 3, D to F. For $f_c = {}^1/_2$, we find $\mu = 1 \pm 0.03$. For both $f_c = 1$ and $f_c = 2$, we find $\mu = 1.2 \pm 0.03$ for all four plots. This universal scaling behavior of $dV(B, I)/dI$ experimentally establishes the existence of the vortex Mott insulator and the dynamic vortex insulator-to-metal transition in superconducting networks.

To gain insight into the observed scaling behaviors, we focus on $f_c = 1$. At $I << I_0$, thermally activated dynamics of vortices is governed by motion of large vortex bundles and occurs via a creep mechanism without breaking the vortex lattice integrity, resulting in $V \propto \exp(-I_0/I)$ (*18*). General creep considerations (*19*) suggest that at some threshold current less than the depinning current, the elastic continuity of the vortex system breaks down and vortex dynamics occurs via the plastic gliding of dislocations. The latter is equivalent to phase slips of the superconducting order parameter resulting in the linear ohmic response (i.e., the metallic behavior). Identifying this plastic threshold current with I_0 leads to the notion that the vortex metal is a phase whose dynamics is controlled by phase slips. Very near the threshold, $I \to I_0$, thermally activated dynamics are governed by activation over a small parabolic barrier whose height scales as $[1 - (I/I_0)]^{3/2}$, giving rise to

$$V \propto \frac{1}{1 + \exp\{\text{const}[1 - (I/I_0)]^{3/2}\}} \quad (2)$$

(*20*). Thus, the characteristic energy controlling the response of the vortex system near the vortex insulator-to-metal transition scales as $|I - I_0|^{3/2}$, which explains the origin of the experimentally observed scaling $|b| \propto |I - I_0|^{3/2}$

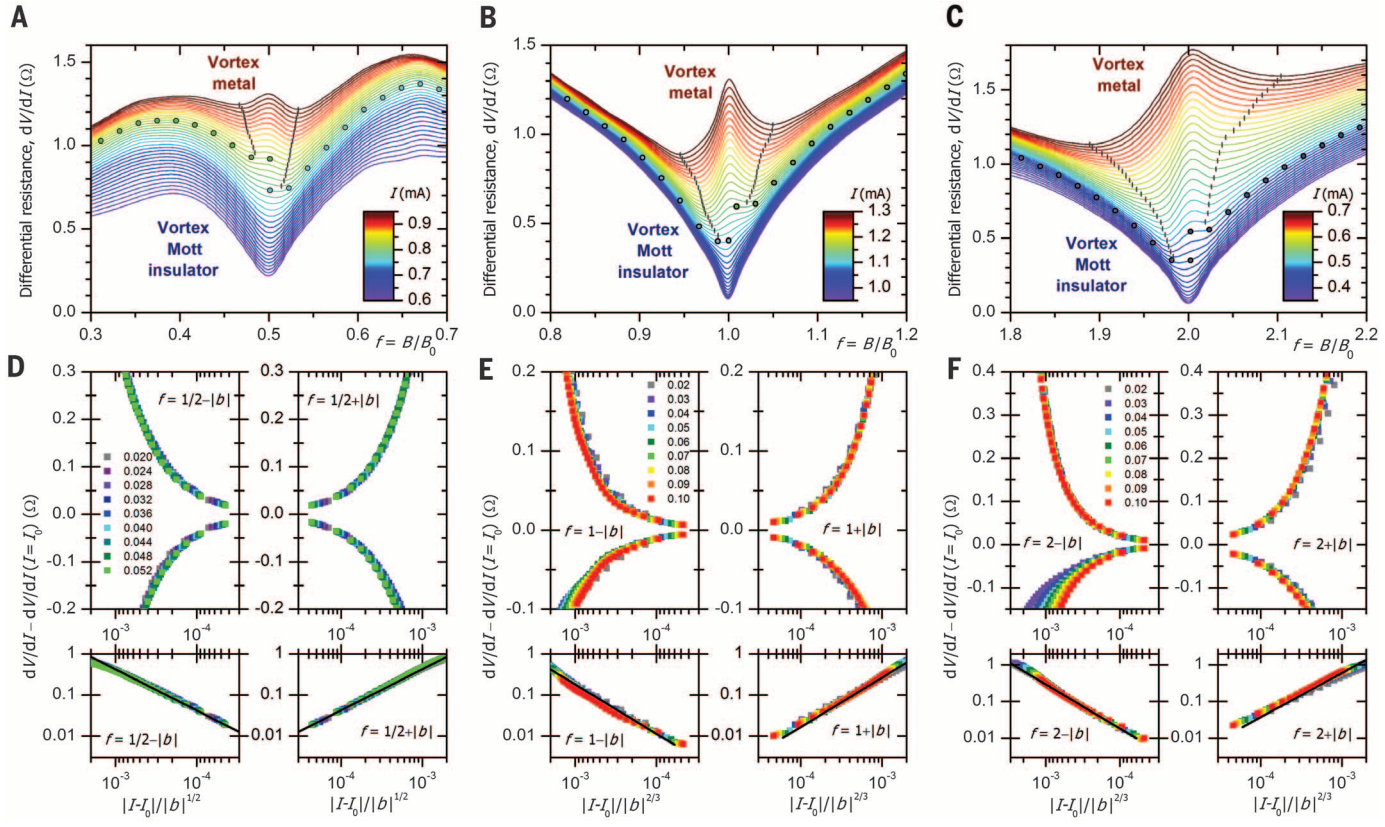

Fig. 3. Scaling at the dynamic vortex Mott insulator-to-metal transition. (**A** to **C**) dV/dI versus f in the vicinity of $f_c = {}^1/_2$, 1, and 2, respectively. Each panel contains 36 traces in 0.01-mA steps. Colors reflect magnitudes of the current. The dots mark $(dV/dI)(I = I_0)$ values separating insulating-like and metallic-like behaviors. The separatrix traces are chosen so that dV/dI values start to turn upward on approach to f_c at $I > I_0$, dV/dI maintains a downward trend near f_c at $I < I_0$, and $d(dV/dI)/df|_{f=f_c} = 0$ at $I = I_0$. In the metallic regions, dV/dI minima marked with strokes enclose the critical regions around f_c. The traces are not symmetric with respect to f_c, so I_0^- and I_0^+ are different: (A) $I_0^- = 0.83$ mA, $I_0^+ = 0.78$ mA; (B) $I_0^- = 1.10$ mA, $I_0^+ = 1.14$ mA; (C) $I_0^- = 0.45$ mA, $I_0^+ = 0.48$ mA. (**D** to **F**) Scaling of the same data after subtracting the corresponding separatrix, $dV/dI - (dV/dI)(I = I_0)$ with respect to variable $|I - I_0|/|b|^{(\delta-1)/\delta}$ with $b = f - f_c$ and $\delta = 2$ for $f_c = {}^1/_2$ (D) and $\varepsilon = {}^2/_3$ for $f_c = 1$ and $f_c = 2$ [(E) and (F)]. Subpanels at left and right show scaling plots in the $f_c - |b|$ and $f_c + |b|$ vicinities of the critical frustration parameters, respectively; the colors refer to different $|b|$ values. Upper panels use the linear scales of $dV/dI - (dV/dI)(I = I_0)$; lower panels use logarithmic scales. The scales are the same for each f_c pairwise for the left and right subpanels. The black lines in the lower panels correspond to powers $\mu = 1$ for $f_c = {}^1/_2$, and to $\mu = 1.2 \pm 0.03$ for $f_c = 1$ and 2.

for integer frustrations. Notably, the observed value of $\varepsilon = {}^{2}/_{3}$ for the integer dynamic transition coincides with the corresponding mean-field value for the temperature- and pressure-driven thermodynamic electronic Mott transition (*21*) belonging in the class of the liquid-gas transition of classical systems (*1*, *21*, *22*). The universal scaling properties of the current- and magnetic field–dependent dynamical resistivity experimentally demonstrate that a vortex Mott insulator undergoes a phase transition resembling a liquid-to-gas transition at the nonequilibrium critical end point. The critical exponent at $f_c = {}^{1}/_{2}$ is $\varepsilon = {}^{1}/_{2}$, indicating that fractional vortex Mott transitions belong in different universality classes.

REFERENCES AND NOTES

1. L. P. Kadanoff *et al.*, *Rev. Mod. Phys.* **39**, 395–431 (1967).
2. M. E. Fisher, *Rev. Mod. Phys.* **46**, 597–616 (1974).
3. M. Henkel, H. Hinrichsen, S. Lübeck, *Non-Equilibrium Phase Transitions* (Springer, New York, 2008).
4. R. S. Newrock, C. J. Lobb, U. Geigenmüller, M. Octavio, *Solid State Phys.* **54**, 263–512 (1999).
5. D. R. Nelson, V. M. Vinokur, *Phys. Rev. B* **48**, 13060–13097 (1993).
6. M. Baert, V. V. Metlushko, R. Jonckheere, V. V. Moshchalkov, Y. Bruynseraede, *Phys. Rev. Lett.* **74**, 3269–3272 (1995).
7. K. Harada *et al.*, *Science* **274**, 1167–1170 (1996).
8. S. Goldberg *et al.*, *Phys. Rev. B* **79**, 064523 (2009).
9. See supplementary materials on *Science* Online.
10. M. Tinkham, D. W. Abraham, C. J. Lobb, *Phys. Rev. B* **28**, 6578–6581 (1983).
11. T. I. Baturina, Yu. A. Tsaplin, A. E. Plotnikov, M. R. Baklanov, *JETP Lett.* **81**, 10–14 (2005).
12. S. Eley, S. Gopalakrishnan, P. M. Goldbart, N. Mason, *Nat. Phys.* **8**, 59–62 (2012).
13. D. R. Hofstadter, *Phys. Rev. B* **14**, 2239–2249 (1976).
14. T. I. Baturina *et al.*, *Europhys. Lett.* **93**, 47002 (2011).
15. S. P. Benz, M. S. Rzchowski, M. Tinkham, C. J. Lobb, *Phys. Rev. B* **42**, 6165–6171 (1990).
16. Z. Jiang, D. A. Dikin, V. Chandrasekhar, V. V. Metlushko, V. V. Moshchalkov, *Appl. Phys. Lett.* **84**, 5371–5373 (2004).
17. M. J. Rozenberg, R. Chitra, G. Kotliar, *Phys. Rev. Lett.* **83**, 3498–3501 (1999).
18. G. Blatter, M. V. Feigel'man, V. B. Geshkenbein, A. I. Larkin, V. M. Vinokur, *Rev. Mod. Phys.* **66**, 1125–1388 (1994).
19. J. Kierfeld, H. Nordborg, V. M. Vinokur, *Phys. Rev. Lett.* **85**, 4948–4951 (2000).
20. L. D. Landau, E. M. Lifshitz, *Quantum Mechanics* (Elsevier, Oxford, 1977)
21. P. Limelette *et al.*, *Science* **302**, 89–92 (2003).
22. G. Kotliar, E. Lange, M. J. Rozenberg, *Phys. Rev. Lett.* **84**, 5180–5183 (2000).
23. P. G. Harper, *Proc. Phys. Soc. A* **68**, 874–878 (1955).

ACKNOWLEDGMENTS

We thank M. Lankhorst, F. Roesthuis, and D. Veldhuis for help during the experiments. Supported by the Dutch FOM and NWO foundations; the U.S. Department of Energy, Office of Science, Materials Sciences and Engineering Division; and Ministry of Education and Science of the Russian Federation grant 14.Y26.31.0007. N.P. and T.I.B. acknowledge for financial support the Marie Curie IEF and the Alexander von Humboldt Foundation, respectively. All data are available in the supplementary materials. Author contributions: N.P. conceived and designed the experiment; N.P., F.C., C.G.M., and X.R.W. performed the experiments; V.M.V. conceived the theoretical concept; T.I.B. and V.M.V. analyzed experimental data and developed a theory; A.A.G., A.B., G.B., and H.H. contributed to the theoretical description; and all authors contributed in writing the manuscript.

SUPPLEMENTARY MATERIALS

www.sciencemag.org/content/349/6253/1202/suppl/DC1
Materials and Methods
Supplementary Text
Figs. S1 and S2
Reference (*24*)

27 August 2014; accepted 29 July 2015
10.1126/science.1260507

QUANTUM MECHANICS

A self-interfering clock as a "which path" witness

Yair Margalit, Zhifan Zhou, Shimon Machluf,* Daniel Rohrlich, Yonathan Japha, Ron Folman†

In Einstein's general theory of relativity, time depends locally on gravity; in standard quantum theory, time is global—all clocks "tick" uniformly. We demonstrate a new tool for investigating time in the overlap of these two theories: a self-interfering clock, comprising two atomic spin states. We prepare the clock in a spatial superposition of quantum wave packets, which evolve coherently along two paths into a stable interference pattern. If we make the clock wave packets "tick" at different rates, to simulate a gravitational time lag, the clock time along each path yields "which path" information, degrading the pattern's visibility. In contrast, in standard interferometry, time cannot yield "which path" information. This proof-of-principle experiment may have implications for the study of time and general relativity and their impact on fundamental effects such as decoherence and the emergence of a classical world.

Two-slit interferometry of quanta, such as photons and electrons, figured prominently in the Bohr-Einstein debates on the consistency of quantum theory (*1*, *2*). A fundamental principle emerging from those debates—intimately related to the uncertainty principle—is that "which path" information about the quanta passing through slits blocks their interference. At the climax of the debates, Einstein claimed that a clock, emitting a photon at a precise time while being weighed on a spring scale to measure the change in its mass-energy, could evade the uncertainty principle. Yet Bohr showed that the clock's gravitational redshift induces enough uncertainty in the emission time to satisfy the uncertainty principle. Inspired by the subtle role that time may play, we have now sent a clock through a spatial interferometer. Our proof-of-principle experiment introduces clock interferometry as a new tool for studying the interplay of general relativity (*3*) and quantum mechanics (*4*).

Time in standard quantum mechanics is a global parameter, which cannot differ between paths. Hence, in standard interferometry (*5*) a difference in height between two paths merely affects their relative phase, shifting their interference pattern without degrading its visibility. In contrast, general relativity predicts that a clock must "tick" slower along the lower path; thus if the paths of a clock through an interferometer have different heights, a time differential between the paths will yield "which path" information and degrade the visibility of the interference pattern (*6*). Consequently, whereas standard interferometry may probe general relativity (*7*–*9*), clock interferometry probes the interplay of general relativity and quantum mechanics. For example, loss of visibility because of a proper time lag would be evidence that gravitational effects contribute to decoherence and the emergence of a classical world (*10*).

Although our interferometer is of a new type, it is worthwhile noting decades of progress in matter-wave interferometry (*11*). Specifically, we note experiments in which neutron spins have been rotated in a magnetic field (*12*, *13*) and experiments in which different paths were labeled (*14*). For completeness, we also note recent work on the so-called Compton clock interferometer (*15*) and the debates that ensued [(*16*, *17*) and references therein].

In our experiment, atomic clocks—atoms in superpositions of internal states—pass through an atomic matter-wave interferometer. We demonstrate that the visibility of interference patterns produced by thousands of self-interfering clocks [atoms in a Bose-Einstein condensate (BEC)] depends on the (simulated) proper time differential between the recombined wave packets of each clock. We simulated the time differential or lag by artificially making one clock wave packet "tick" faster than the other. Although our clock is not accurate enough to be sensitive to special- or general-relativistic effects, it is able to demonstrate that a differential time reading affects the visibility of a clock self-interference pattern (*6*); specifically, the visibility equals the scalar product of the interfering clock states.

In principle, any system evolving with a well-defined period can be a clock. We used a quantum two-level system: a ^{87}Rb atom in a superposition of two Zeeman sublevels, the $m_F = 1$ and $m_F = 2$ sublevels of the $F = 2$ hyperfine state.

The general scheme of the clock interferometer is shown in Fig. 1 (*18*). To prepare the clock in a superposition of two different locations, we made use of the previously demonstrated Stern-Gerlach type matter-wave interferometer on an atom chip (*19*), creating a coherent spatial superposition of a ^{87}Rb BEC (~10^4 atoms) 90 μm below the chip surface. Initially, after the application of a field gradient beam splitter (FGBS) and a stopping pulse that zeroes the relative velocity of

Department of Physics, Ben-Gurion University of the Negev, Beer-Sheva 84105, Israel.
*Present address: Van der Waals-Zeeman Institute, University of Amsterdam, Science Park 904, 1090 GL Amsterdam, Netherlands.
†Corresponding author. E-mail: folman@bgu.ac.il

Critical behavior at a dynamic vortex insulator-to-metal transition

Nicola Poccia, Tatyana I. Baturina, Francesco Coneri, Cor G. Molenaar, X. Renshaw Wang, Ginestra Bianconi, Alexander Brinkman, Hans Hilgenkamp, Alexander A. Golubov and Valerii M. Vinokur

Science **349** (6253), 1202-1205.
DOI: 10.1126/science.1260507

Vortices in a superconducting egg crate

Near equilibrium phase transitions, physical systems that bear no resemblance to one another can behave in a very similar way. For example, thermodynamic functions follow the same scaling behavior in a magnetic transition as in the seemingly unrelated gas-liquid transition. Does such universality exist in nonequilibrium phase transitions? Poccia *et al.* fabricated a square array of superconducting islands on a metallic surface. They applied a magnetic field, which caused vortices to form in between the islands, and induced a transition from a state in which vortices were stuck to their positions to one where they were able to move. They observed the same scaling behavior that applies to some equilibrium transitions.

Science, this issue p. 1202